Appendix B

Techniques for Analyzing Footpoint Asymmetries in the 2003-10-29 X10 Flare (Chapter 5)

In this appendix we describe the techniques used in Chapter 5 to analyze the footpoint asymmetries in the 2003 October 29 X10 flare, including coalignment of images obtained by different instruments (§B.1), a mathematical treatment of column density asymmetry (§B.2), and an estimate of the density in the legs of the loop (§B.3).

B.1 Coalignment of Images from Different Instruments

We describe in this section the procedures that were taken to coalign images[1] obtained by different instruments shown in §5.2.3. It was assumed that images from all instruments had accurate plate scales and roll angles were corrected for the solar P-angle, but had different absolute origins for the x and y coordinates. *RHESSI*'s images are located on the Sun to sub-arcsecond accuracy thanks to its solar limb sensing aspect system and star based roll angle measurements (Fivian et al., 2002). Thus all other images were corrected to match the *RHESSI* features using the following procedures.

(1) We first obtained an accurate coalignment of *SOHO* MDI with *RHESSI*, which is important for our purpose to find the magnetic field strength at the HXR FPs.

(1.1) The first step is to identify specific features on the MDI map that have *RHESSI* counterparts. Qiu & Gary (2003) found good spatial agreement between HXR FPs and MDI magnetic anomaly features with an apparent sign reversal in a white-light flare. This was interpreted as HXR-producing nonthermal electrons being responsible for heating the lower atmosphere, which consequently altered the Ni I 6768 Å line profile that is used by MDI to measure the magnetic field.

We selected two neighboring magnetograms at 20:41:35 and 20:42:35 UT when the magnetic anomaly features were most pronounced, and subtracted the former from the latter. This running-differenced map (which we call map_0, Fig. B.1) highlights regions of the newest

[1] See P. Gallagher's tutorial for coaligning images at http://hesperia.gsfc.nasa.gov/∼ptg/trace-align

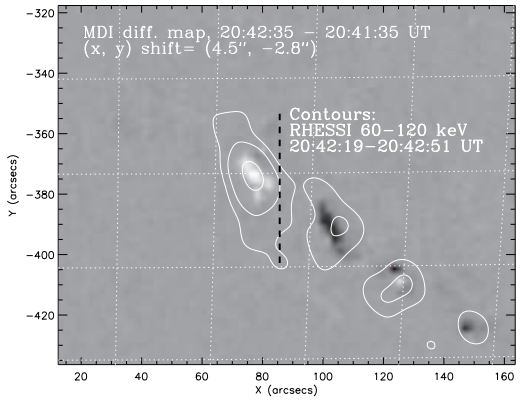

Figure B.1: Difference (*gray background*) between two MDI magnetograms at 20:42:35 and 20:41:35 UT, overlaid with a *RHESSI* 60–120 keV image at 20:42:19–20:42:51 UT (white contours at 15%, 30%, & 80% of the maximum brightness). The MDI differenced magnetogram has been corrected to an Earth-centered view and shifted in x and y to give the best fit to the four *RHESSI* HXR sources (see text). For display purposes only, we also did the solar rotation correction to the fiducial *TRACE* time of 20:50:42 UT as we did for Fig. 5.6*a*, and the vertical dark dashed line shows the same general magnetic neutral line as shown there [from Liu, W. et al. 2008a].

changes, which are presumably caused by precipitation of nonthermal electrons and are expected to appear cospatial with HXR sources. As evident, there is one (three) apparent increase (decrease) feature(s) mainly in the negative (positive) polarity (cf., Fig. 5.6), which appear as *white* (*dark*) patches in Figure B.1. Meanwhile, we reconstructed a *RHESSI* image (called map_1) at 60–120 keV integrated in the interval of 20:42:19–20:42:51 UT (a multiple of the *RHESSI* spin period, ∼4 s, and closest to the corresponding integration time of the second MDI magnetogram, 20:42:20–20:42:50 UT). We found an one-to-one correspondence between the four major HXR FP sources (Fig. B.1, *contours*) and the magnetic anomalies.

(1.2) The second step is to convert *SOHO*'s L1 view to the appearance as viewed from an Earth orbit. In principle, for the best accuracy, one could use a routine called *mk_soho_map_earth.pro* developed by T. Metcalf in the Solar SoftWare (SSW) package, which reads *SOHO* orbital data and involves complicated trigonometry and warping. Its results, however, were unstable and introduced artificial pointing jumps. Thus, we used a simpler, but less accurate, routine called *map2earth.pro* developed by D. Zarro, which only corrects for the pixel size of the map according to different distances from the Sun to the L1 point and to the Earth. We call the resulting Earth-viewed differenced MDI magnetogram $map_{0,\,\mathrm{Earth}}$.

(1.3) Finally, we took the absolute values of MDI $map_{0,\,\mathrm{Earth}}$ to make a new map called $map'_{0,\,\mathrm{Earth}}$ and coregister it with the corresponding *RHESSI* map_1 by cross-correlation. The required pointing shifts for MDI are $\Delta x = 4.5'' \pm 2.0''$ and $\Delta y = -2.8'' \pm 2.0''$. This practical approach yielded the best coalignment between MDI and *RHESSI*, and also resolved the inaccuracy caused by negligence of *SOHO* orbital data in the *map2earth.pro* routine. Here we estimate the uncertainty with the $2.0''$ MDI pixel size and use error propagation with the corresponding pixel sizes for the following coalignments with other instruments.

(2) Following a similar practice, we cross-correlated the *TRACE* white light image at

20:49:49 UT (Fig. 5.6*c*) with an MDI magnetogram[2] at 20:49:35 UT and found that the *TRACE* image (pixel size 0.5″) must be shifted by $\Delta x = 2.2''$ and $\Delta y = 0.0''$. Considering the MDI offset estimated above, this translates to a required shift of $\Delta x = 2.2 + 4.5 = 6.7'' \pm 2.1''$ and $\Delta y = 0.0 - 2.8 = -2.8'' \pm 2.1''$ for *TRACE* to match *RHESSI*'s pointing. These shifts were applied to all the *TRACE* images shown in Figure 5.6, assuming they shared a common pointing that did not change during the flare.

(3) To find the correct pointing for the OSPAN Hα image (pixel size 2.2″) at 20:42:11 UT (Fig. 5.6*b*), we used the concurrent *TRACE* 1600 Å image (20:42:11 UT) as the reference. Cross-correlation between the two images indicated that the former must be shifted by $\Delta x = -1.0''$ and $\Delta y = 6.6''$. Using the above relative *TRACE* pointing, we found the shifts of $\Delta x = -1 + 6.7 = 5.7'' \pm 3.0''$ and $\Delta y = 6.6 - 2.8 = 3.8'' \pm 3.0''$ required for this Hα image.

B.2 Derivation of Footpoint HXR Fluxes Resulting from Asymmetric Coronal Column Densities

Here we derive the numerical expressions for the HXR fluxes of the two FPs and their ratio as a function of energy resulting from column density asymmetry addressed in §5.5.2. We adopted the empirical expression of Leach & Petrosian (1983, their eq. (11)) for nonthermal bremsstrahlung X-ray emission as a function of column density, which has also been used in Chapter 6 [see eq. (6.5)]. This expression well approximates the Fokker-Planck calculation of particle transport under the influence of Coulomb collisions that includes energy losses and pitch-angle scattering, the latter of which was neglected in other forms of X-ray profiles based on approximate analytical solutions (e.g., Emslie & Machado, 1987). For an injected power-law (index δ) electron flux, the resulting fractional bremsstrahlung emission intensity per unit dimensionless column density τ at photon energy k (in units of rest electron energy $m_e c^2 = 511$ keV, m_e being the electron mass) can be written as

$$I_0(\tau, k) = \left(\frac{\delta}{2} - 1\right) \left(\frac{k+1}{gk^2}\right) \left(1 + \tau \frac{k+1}{gk^2}\right)^{-\delta/2} , \tag{B.1}$$

where $\tau = N[4\pi r_0^2 \ln \Lambda] = N/[5 \times 10^{22}\,\mathrm{cm}^{-2}]$ is the dimensionless column density, for the classical electron radius $r_0 = e^2/m_e c^2 = 2.8 \times 10^{-13}$ cm and the Coulomb logarithm $\ln \Lambda = 20$; g is a factor determined by the pitch-angle distribution of the injected electron spectrum, which we assumed to be isotropic and thus $g = 0.37$ (Leach, 1984). This emission profile is normalized to unity, $\int_0^\infty I_0(\tau, k) d\tau = 1$. Integrating equation (B.1) yields the cumulative photon emission from the injection site ($\tau = 0$) to the transition region ($\tau = \tau_{\rm tr} \equiv N_{\rm tr}/[5 \times 10^{22}\ \mathrm{cm}^{-2}]$, where $N_{\rm tr} = \int_0^{s_{\rm tr}} n[s] ds$ and $s_{\rm tr}$ are the coronal column density and distance to the transition region),

$$F_{\rm Corona}(\tau_{\rm tr}) = \int_0^{\tau_{\rm tr}} I_0(\tau, k) d\tau = 1 - \left(1 + \tau_{\rm tr} \frac{k+1}{gk^2}\right)^{1-\delta/2} , \tag{B.2}$$

[2]It would have been preferable to use an MDI white-light image, but none was recorded during the flare.

whose complement gives the emission accumulated below the transition region, i.e., the HXR flux of the FP,

$$F_{\rm FP}(\tau_{\rm tr}) = \int_{\tau_{\rm tr}}^{\infty} I_0(\tau,k)d\tau = 1 - F_{\rm Corona}(\tau_{\rm tr}) = \left(1+\tau_{\rm tr}\frac{k+1}{gk^2}\right)^{1-\delta/2}. \quad \text{(B.3)}$$

Note that at large photon energies (tens to hundreds of keV), $F_{\rm Corona}(\tau_{\rm tr})$ is usually much smaller than $F_{\rm FP}(\tau_{\rm tr})$. In addition, $F_{\rm Corona}(\tau_{\rm tr})$ is distributed in a large volume in the leg of the loop in the relatively *tenuous* plasma, while $F_{\rm FP}(\tau_{\rm tr})$ is concentrated at the FP in the *dense* transition region and chromosphere. This results in an even smaller surface brightness in the leg than at the FP, which may well exceed the dynamic range of HXR telescopes (e.g., $\gtrsim$10:1 for *RHESSI*). This is why leg emission is so rarely observed (Liu, W. et al., 2006; Sui et al., 2006).

As we know, a power-law electron flux (index=δ) produces a thick-target (integrated from $\tau = 0$ to $\tau = \infty$) photon spectrum of approximately a power-law, $I_{\rm thick} = A_0 k^{-\gamma}$, where $\gamma = \delta - 1$ (Brown, 1971; Petrosian, 1973) for an isotropically injected electron spectrum, and A_0 is the normalization factor [in units of photons $\rm s^{-1}$ $\rm cm^{-2}$ $(511\,\rm keV)^{-1}$]. Since I_0 gives the fractional spatial photon distribution at a given energy, the physical photon spectrum at energy k and at a depth where the overlying column density is τ can be written as $I(\tau,k) = I_{\rm thick} I_0(\tau,k) = A_0 k^{-\gamma} I_0(\tau,k)$. It follows that the X-ray flux of the FP is

$$I_{\rm FP}(\tau_{\rm tr},k) = \int_{\tau_{\rm tr}}^{\infty} I(\tau,k)d\tau = I_{\rm thick} F_{\rm FP}(\tau_{\rm tr}) = A_0 k^{-\gamma}\left(1+\tau_{\rm tr}\frac{k+1}{gk^2}\right)^{1-\delta/2}, \quad \text{(B.4)}$$

and the photon flux ratio of the two FPs (1 and 2),

$$R_I = \frac{I_{\rm FP}(\tau_{\rm tr,2},k)}{I_{\rm FP}(\tau_{\rm tr,1},k)} = \left(1+\tau_{\rm tr,2}\frac{k+1}{gk^2}\right)^{1-\delta/2}\left(1+\tau_{\rm tr,1}\frac{k+1}{gk^2}\right)^{-(1-\delta/2)}. \quad \text{(B.5)}$$

The above two equations were used in §5.5.2 to calculate the FP fluxes and their ratio resulting from different coronal column densities.

B.3 Estimation of Column Densities in Loop Legs

We describe below the approach to estimate the coronal column densities $N_{\rm tr}$ in the legs of the loop, which is defined and used in §5.5.2 as the density integrated along the loop from the acceleration region to the transition region at the FPs. In the stochastic acceleration model of Petrosian & Liu (2004), the LT source is the region where particle acceleration takes place (Liu, W. et al., 2008b; Xu et al., 2008). We thus subtracted[3] the estimated LT size (i.e., the radius r of the *equivalent sphere*; see Fig. 5.5*c*) from the distances along the loop from the LT centroid to the FP centroids obtained in §5.4.2 (i.e., l_i, where i=1 for E-FP and 2 for W-FP; see Fig. 5.7*c*), to obtain the path lengths in the legs $s_{{\rm tr},i} = l_i - r$.

[3]In some other models (e.g., Masuda et al., 1994), the acceleration region is assumed to be located above the "LT" source and a distance needs to be added to l_i. Such a practice was not attempted here, and as we can see from §5.5.2, will not change our conclusions.

Here the FP centroids are assumed to be situated at negligibly small distances below the transition region. To give the desired column densities $N_{\mathrm{tr},\,i}$, the path lengths $s_{\mathrm{tr},\,i}$ (i=1, 2) were then multiplied by the density n_{leg} (assumed to be uniform) in the legs of the loop, which was estimated as follows.

The density of the LT source n_{LT} inferred in §5.2.2 (see Fig. 5.5*d*) provides our first guess for the leg density n_{leg} as assumed by Falewicz & Siarkowski (2007). The relative brightness of *nonthermal* bremsstrahlung emission the leg and FP provides another important clue. This is because, for the same reason of collisional losses mentioned in §5.5.2, the ratio of the leg to FP brightness, particularly at low energies, is an increasing function of the leg density. This predicted ratio cannot exceed the observed LT-to-FP brightness ratio, because the LT source is where the maximum loop brightness is located, and it includes additional contributions from *thermal* emission, piled-up photons, and/or electrons trapped in the acceleration region (Petrosian & Liu, 2004). This imposes an upper limit for the leg density n_{leg}.

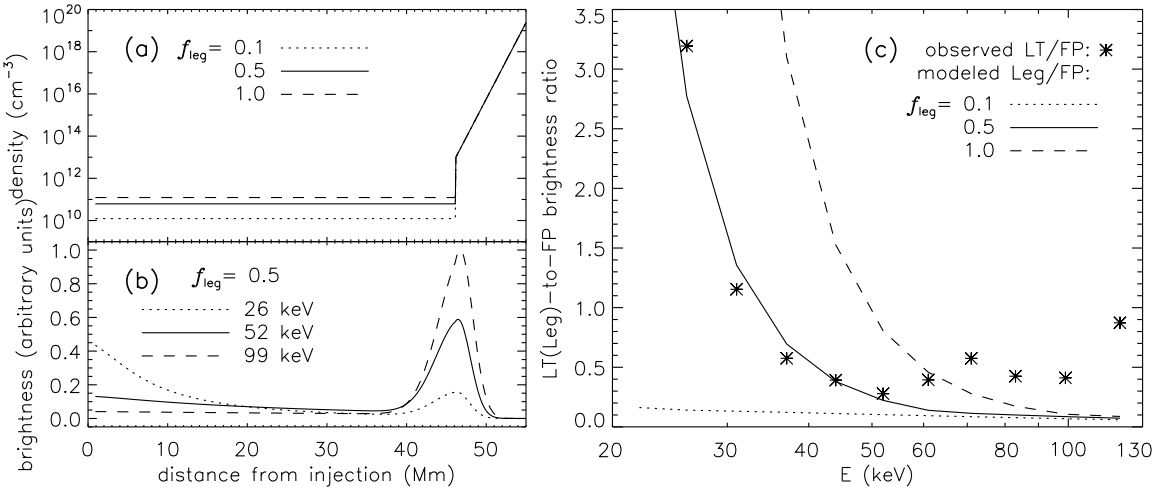

Figure B.2: (*a*) Density vs./ distance s along the loop for different values of the scaling factor f_{leg}, which is applied to the LT density $n_{\mathrm{LT}} = 1.2 \times 10^{11}\,\mathrm{cm}^{-3}$ to give the leg density $n_{\mathrm{leg}} = f_{\mathrm{leg}} n_{\mathrm{LT}}$ (see text). The distance starts at the injection from the acceleration region, and the transition region is located at $s = 46$ Mm. (*b*) Nonthermal emission profiles as seen by *RHESSI* at selected energies. These are produced by a power-law electron flux (index $\delta = 4.96$) injected into the loop with the density profile shown in (*a*) for the case of $f_{\mathrm{leg}} = 0.5$. The humps on the right are the FP emission. (*c*) Observed ratio of the LT-to-FP maximum brightness (*asterisk*) as a function of energy, overlaid with the modeled leg-to-FP ratio (*lines*) for different density profiles shown in (*a*). Above ∼50 keV the abnormal increase of the observed ratio with energy is unreal due to increasing noise at higher energies.

To estimate this upper limit for n_{leg}, we selected the second last long integration interval (20:54:40–20:56:40 UT) shown in Figure 5.8*d* when the loop column density has become large late in the flare and yet the HXR flux is not too low to give sufficient count statistics for images. (1) From images at different energies we obtained the *observed* ratio of the maximum brightness of the LT source to that of the dimmer W-FP source, which is a decreasing function of energy as shown in Figure B.2*c*. (2) The next step was to calculate

the *modeled* leg to FP brightness ratio: (*a*) We assumed a piecewise density profile $n(s)$ consisting of an l_2 long leg with a uniform density of $n_{\rm leg} = f_{\rm leg} n_{\rm LT}$ (where $f_{\rm leg}$ is a scaling factor to be determined), a jump to $10^{13}\,{\rm cm}^{-3}$ at the transition region ($s = l_2$), and an exponential increase with a scale height of 0.6 Mm (given by an assumed temperature of 10^4 K) in the chromosphere (see Fig. B.2*a*). (*b*) Assuming a power-law electron flux with a spectral index of δ injected at the upper end of the leg ($s = 0$), the modeled nonthermal HXR profile was given by $n(s) I_0(\tau, k; \delta)$, where I_0 is defined by equation (B.1). Here we have used the values of $l_2 = 46$ Mm, $n_{\rm LT} = 1.2 \times 10^{11}\,{\rm cm}^{-3}$, and $\delta = 4.96$ from the observation at 20:54:40–20:56:40 UT. (*c*) The modeled emission profile was then convolved with a Gaussian of FWHM=9.8″ corresponding to the CLEAN beam size used for detectors 3–9. A sample of the emission profiles is shown in Figure B.2*b*. (*d*) From the resulting profile, the modeled ratio of the leg-to-FP maximum brightnesses was obtained and compared with the observed ratio (see, e.g., Fig. B.2*c*). (3) To find the upper limit for the scaling factor $f_{\rm leg}$, we started with $f_{\rm leg} = 1$ and iterated the above steps (*a*)–(*d*) with decreasing values at a step of 0.05, until the modeled ratio best fits the the observed ratio as a function of energy in a least-squares sense. This gave us $f_{\rm leg,\,max} = 0.5$, which was then used for the upper limits of the leg density $n_{\rm leg,\,max} = f_{\rm leg,\,max} n_{\rm LT}$ and column densities $N_{{\rm tr},\,i} = n_{\rm leg,\,max}(l_i - r)$ shown in Figure 5.8*e* throughout the flare. This scaling means that the average density in the legs must be smaller than the estimated LT density. Another possibility is that the LT density inferred is an overestimate due to an underestimate of the volume, because of the choice of the 50% contour level (see §5.2.2) which may be too high, or because of the lack of knowledge of the source size in the third dimension along the line of sight.